Chinese Journal of Aeronautics, (2015), 28(4): 1163–1177

Chinese Society of Aeronautics and Astronautics
& Beihang University

Chinese Journal of Aeronautics

cja@buaa.edu.cn
www.sciencedirect.com

UAV feasible path planning based on disturbed fluid and trajectory propagation

Yao Peng, Wang Honglun *, Su Zikang

School of Automation Science and Electrical Engineering, Beihang University, Beijing 100191, China
Unmanned Aerial Vehicle Research Institute, Beihang University, Beijing 100191, China

Received 29 September 2014; revised 28 March 2015; accepted 4 May 2015
Available online 22 June 2015

KEYWORDS

Disturbed fluid;
Feasibility;
Three-dimensional (3-D) path planning;
Trajectory propagation;
Unmanned aerial vehicle (UAV)

Abstract In this paper, a novel algorithm based on disturbed fluid and trajectory propagation is developed to solve the three-dimensional (3-D) path planning problem of unmanned aerial vehicle (UAV) in static environment. Firstly, inspired by the phenomenon of streamlines avoiding obstacles, the algorithm based on disturbed fluid is developed and broadened. The effect of obstacles on original fluid field is quantified by the perturbation matrix, where the tangential matrix is first introduced. By modifying the original flow field, the modified one is then obtained, where the streamlines can be regarded as planned paths. And the path proves to avoid all obstacles smoothly and swiftly, follow the shape of obstacles effectively and reach the destination eventually. Then, by considering the kinematics and dynamics equations of UAV, the method called trajectory propagation is adopted to judge the feasibility of the path. If the planned path is unfeasible, repulsive and tangential parameters in the perturbation matrix will be adjusted adaptively based on the resolved state variables of UAV. In most cases, a flyable path can be obtained eventually. Simulation results demonstrate the effectiveness of this method.

1. Introduction

Path planning refers to plan an optimal path from the starting point to the destination while avoiding obstacles. It is one of the key technologies to improve the autonomy level of unmanned aerial vehicle (UAV). And the planned path should satisfy the following conditions: ① safety, i.e., UAV can avoid all obstacles successfully; ② feasibility, i.e., the planned path should satisfy dynamic constraints and can be tracked by the control system; ③ optimization, i.e., the optimal path is obtained by minimizing the cost function; ④ high computational efficiency, i.e., the complexity of the algorithm is acceptable. Traditional methods usually focus on two-dimensional (2-D) path planning, which is easy to achieve. However, with the development of UAV maneuverability and the demands for low-altitude and terrain-following flight, three-dimensional (3-D) path planning is gaining increasing attention.

* Corresponding author at: School of Automation Science and Electrical Engineering, Beihang University, Beijing 100191, China. Tel.: +86 10 82317546.
E-mail addresses: yaopenghappy@163.com (P. Yao), hl_wang_2002@126.com (H. Wang).
Peer review under responsibility of Editorial Committee of CJA.

Production and hosting by Elsevier

http://dx.doi.org/10.1016/j.cja.2015.06.014

Traditional geometric approaches, based on searching waypoints in digital maps, are improved to solve the 3-D path planning problem. The upgrade of Dubins method[1] extends the Dubins car with altitude. And the time-optimal trajectories are characterized through the Pontryagin maximum principle. Probabilistic roadmaps (PRMs) and D* Lite[2] are combined for path planning with stereo-based occupancy mapping. The improved rapidly-exploring random tree (RRT)[3] produces a time parameterized set of control inputs to make UAV move from the initial point to the destination, which proves to be efficient for 3-D path planning. However, the calculation of these geometric algorithms tends to increase exponentially if the planning space enlarges. Besides, the planned path may be not smooth enough for UAV to track.

Methods based on potential field are utilized to meet the real-time requirements of path planning. Artificial potential field (APF) method[4–7] has the advantages of simple principle and small amount of computation. Yet local minimum exists when the vehicle enters into a concave area. Besides, there may be some oscillation of the path if it enters into the narrow gap between two obstacles. Virtual force (VF) method[8,9] is utilized for real-time path planning. The agent is taken as a particle in 3-D environment and the resultant force consists of two parts: the attractive force pointing to the target point and the repulsive one forcing UAV away from obstacles. The biggest advantage of this method is its ability of real-time computation. However, the definition of repulsive force is not objective enough as it ignores the shape of obstacles. Besides, it is hard to obtain a feasible path sometimes even if the magnitude of attractive or repulsive force is regulated.

The intelligent algorithms, e.g., particle swarm optimization (PSO),[10] evolutionary algorithms (EA)[11] and ant colony algorithm (ACO)[12] are also widely used to plan the optimal path by minimizing the cost function. These methods can be easily employed in different scenarios, but it is possible to trap in a local optimum. Meanwhile, the process of optimization is time-consuming. Therefore, the intelligent methods are improved or combined with other methods to relieve the abovementioned drawback.[13–16] By combing the improved differential evolution method and the level comparison algorithm,[13] an optimal path is eventually obtained in 3-D environment. Pehlivanoglu[16] proposed the multi-frequency vibrational genetic method for path planning, where the initial population is defined by the clustering method and Voronoi diagram. However, the computation efficiency of these intelligent algorithms remains unsatisfactory, especially in 3-D complex environment. Besides, the distance between the adjacent waypoints by these methods is too large, making the planned path unsmooth. As a result, extra strategy of smoothing path is usually needed.

In addition, many novel methods are proposed in order to plan a feasible or smooth path. A novel dynamic system approach[17] is presented for real-time obstacle avoidance and the parameterized modulation of the dynamical system increases the agent's reactiveness, but this method is more suitable for robotic platform. Maneuver-based motion planning method[18] generates a set of trim states and the corresponding maneuver paths, which are based on UAV nonlinear dynamic model and performance constraints. By generating the trim-maneuver library, the complicated path planning is then turned into a simple hybrid optimization problem. Yet only discrete and finite design variables are offered here. The core paths graph (CPG) algorithm[19] calculates the CPG where arcs are minimum-length trajectories satisfying geometrical constraints, and searches the optimal trajectory between two arbitrary nodes of the graph. However, multiple quadratics should be resolved, resulting in low computational efficiency.

In recent years, one kind of methods based on fluid computation[20–23] is gaining more attention because of the planned smooth paths. The path can be generated by two ways:[20,21] the analytical method, which has small amount of calculation but only applies to sphere obstacle; the numerical method, which applies to cases with various obstacles but has the time-consuming drawback. In our previous work, a novel bio-inspired approach based on interfered fluid dynamical system (IFDS)[24,25] is presented for path planning. Unlike other bio-inspired methods, the biggest advantage of this method is its high computational efficiency and smooth planned paths. This method imitates the phenomenon that water in river avoids rocks smoothly and reaches the destination eventually. As the streamlines obtained by simple formula still have certain optimizing properties, they can be available as planned paths for UAV. However, the distribution of streamlines is not wide enough, and therefore sometimes it is hard to obtain a feasible path, even if the reaction parameter is adapted. Besides, the aircraft dynamics are not taken into account.

To solve the above problems, the method based on disturbed flow is developed to generate more widely distributed streamlines by combing the VF method[8] and the interfered fluid dynamical system.[24] Although the physical characteristics of the modified streamlines are broadened, they still conform to the basic properties of fluid flow, i.e., smoothness, impenetrability and accessibility. Therefore, what we only focus on is to adjust repulsive or tangential parameters when the planned path is unfeasible sometimes. Considering most algorithms do not fully consider UAV dynamics and kinematics, trajectory propagation[26,27] is employed here to judge the feasibility of path and to adjust parameters adaptively.

2. Environment modeling

Fig. 1 illustrates a very common phenomenon in the nature: when there are no rocks in the river, water can flow towards the destination straightly; when there are some rocks, running water can still avoid them smoothly and reach the destination eventually. There are some commonalities between this phenomenon and path planning problem. Inspired by this observation, the simple rules are imitated in this paper to solve UAV path planning problem: rocks in river are regarded as

Fig. 1 Running water avoiding rocks.

obstacles in UAV flight environment; the straight running water is the original fluid field, where the straight streamlines are taken as the initial paths; the deflected running water is regarded to be the disturbed fluid, where the modified streamlines are taken as the planned paths.

2.1. Obstacle modeling

UAV is obliged to avoid obstacles in real flight environment, e.g., mountains, buildings, radars and antiaircraft fires.[28,29] In this paper, each obstacle is described approximately as a standard convex object to simplify the algorithm: a standalone hill is equivalent to a cone; a tall building can be regarded as a parallelepiped; the radar is formulated as a hemisphere; antiaircraft fire can be expressed as a cylinder.

A unified formulation is utilized for obstacle modeling. We define the coordinate system o-xyz as the planning space. $\xi = (x, y, z)$ is taken as UAV position. Suppose the convex object centers at $\xi_0 = (x_0, y_0, z_0)$ with axis lengths a, b, c and index parameters d, e, f. Then we can construct the function

$$F(\xi) = \left(\frac{x - x_0}{a}\right)^{2d} + \left(\frac{y - y_0}{b}\right)^{2e} + \left(\frac{z - z_0}{c}\right)^{2f} \tag{1}$$

Parameters a, b, c, d, e and f determine the shape and size of the obstacle: if $a = b = c$ and $d = 1,\ e = 1,\ f = 1$, the obstacle is a sphere; if $a = b$ and $d = 1,\ e = 1,\ 0 < f < 1$, the obstacle is regarded as a cone; if a and b are variables meeting the condition $a = b = R_1 + (R_2 - R_1)z/c$ and $d = 1$, $e = 1$, $f > 1$ holds, the obstacle is a circular truncated cone approximately, where R_1 and R_2 are radii of two bases.

2.2. Original fluid

If there are no obstacles in flight environment, the original streamlines, i.e., UAV paths are supposed to be straight lines from the start points to the target point with a constant velocity. Suppose that the destination is $\xi_d = (x_d, y_d, z_d)$ and the cruising speed of UAV is a constant C, then the original fluid velocity can be described as

$$\boldsymbol{v}(\xi) = \left[\frac{C(x - x_d)}{d(\xi)}, \frac{C(y - y_d)}{d(\xi)}, \frac{C(z - z_d)}{d(\xi)}\right]^{\mathrm{T}} \tag{2}$$

where $d(\xi) = \sqrt{(x - x_d)^2 + (y - y_d)^2 + (z - z_d)^2}$ is the distance between ξ and ξ_d.

2.3. Disturbed fluid

The influence of rocks on water, i.e., the effect of obstacles on the original fluid, can be quantified by the perturbation matrix $\boldsymbol{P}(\xi)$. Then, by modulating the original fluid velocity, the disturbed fluid velocity can be obtained. The detailed steps will be described in Sections 3 and 4.

Fig. 2(a) illustrates the original flow from a series of start points to the only target point $(5, 5, 0)$. In Fig. 2(b), scenario 1 with three sphere obstacles is constructed, and the effect on original flow is illustrated. Fig. 2(c) illustrates the interfered streamlines in scenario 2, where one sphere, one cylinder and one cone obstacle exist. It can be seen that the modified streamlines will avoid the obstacles smoothly, follow the shape of obstacles effectively and reach the destination eventually.

3. Path planning for a single obstacle

3.1. Algorithm description

Based on the description in Section 2, the procedures of path planning are as follows: first, the perturbation matrix $\boldsymbol{P}(\xi)$ is computed; then we calculate the disturbed fluid velocity $\bar{\boldsymbol{v}}(\xi)$ by modifying the original flow velocity $\boldsymbol{v}(\xi)$; Finally, the disturbed streamline, i.e., the planned path is obtained by the recursive integration of $\bar{\boldsymbol{v}}(\xi)$. The calculation of $\boldsymbol{P}(\xi)$ is the crux in this paper.

Suppose the start point is $\xi_s = (x_s, y_s, z_s)$. To describe the influence of obstacle on the original flow, the perturbation matrix $\boldsymbol{P}(\xi)$ is defined as

$$\boldsymbol{P}(\xi) = \boldsymbol{I} - \frac{\boldsymbol{n}(\xi)\boldsymbol{n}(\xi)^{\mathrm{T}}}{|F(\xi)|^{\frac{1}{\rho(\xi)}}\boldsymbol{n}(\xi)^{\mathrm{T}}\boldsymbol{n}(\xi)} + \frac{\tau\boldsymbol{t}(\xi)\boldsymbol{n}(\xi)^{\mathrm{T}}}{|F(\xi)|^{\frac{1}{\sigma(\xi)}}\|\boldsymbol{t}(\xi)\|\|\boldsymbol{n}(\xi)\|} \tag{3}$$

where $\boldsymbol{I}$ is a 3×3 identity matrix, $\boldsymbol{n}(\xi)$ the normal vector, $\boldsymbol{t}(\xi)$ defined as the tangential vector and τ a saturation function defining the orientation of tangential velocity; $\|\cdot\|$ is 2-norm of a vector or a matrix. Besides, $\rho(\xi)$ and $\sigma(\xi)$ can determine the weight of $\boldsymbol{n}(\xi)$ and $\boldsymbol{t}(\xi)$ respectively. $\boldsymbol{n}(\xi)$, $\boldsymbol{t}(\xi)$, $\rho(\xi)$, $\sigma(\xi)$ and τ are defined respectively as follows:

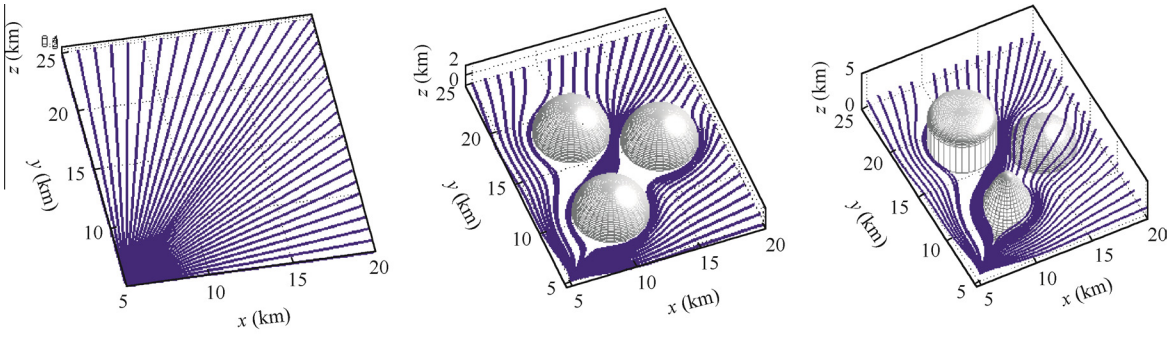

(a) Original fluid (b) Modified fluid in scenario 1 (c) Modified fluid in scenario 2

Fig. 2 Modification of flow.

$$\boldsymbol{n}(\xi)=\left[\frac{\partial F(\xi)}{\partial x},\frac{\partial F(\xi)}{\partial y},\frac{\partial F(\xi)}{\partial z}\right]^{\mathrm{T}} \tag{4}$$

$$\boldsymbol{t}(\xi)=\left[\frac{\partial F(\xi)}{\partial y},-\frac{\partial F(\xi)}{\partial x},0\right]^{\mathrm{T}} \tag{5}$$

$$\rho(\xi)=\rho_0\exp\left(1-\frac{1}{d_0(\xi)d(\xi)}\right) \tag{6}$$

$$\sigma(\xi)=\sigma_0\exp\left(1-\frac{1}{d_0(\xi)d(\xi)}\right) \tag{7}$$

$$\tau=\begin{cases}1 & \boldsymbol{v}(\xi)^{\mathrm{T}}\boldsymbol{t}(\xi)\boldsymbol{n}(\xi)^{\mathrm{T}}\boldsymbol{v}(\xi)>\bar{\varepsilon}\\ \dfrac{\boldsymbol{v}(\xi)^{\mathrm{T}}\boldsymbol{t}(\xi)\boldsymbol{n}(\xi)^{\mathrm{T}}\boldsymbol{v}(\xi)}{\bar{\varepsilon}} & -\bar{\varepsilon}\leqslant\boldsymbol{v}(\xi)^{\mathrm{T}}\boldsymbol{t}(\xi)\boldsymbol{n}(\xi)^{\mathrm{T}}\boldsymbol{v}(\xi)\leqslant\bar{\varepsilon}\\ -1 & \boldsymbol{v}(\xi)^{\mathrm{T}}\boldsymbol{t}(\xi)\boldsymbol{n}(\xi)^{\mathrm{T}}\boldsymbol{v}(\xi)<-\bar{\varepsilon}\end{cases} \tag{8}$$

where ρ_0 is the repulsive parameter, σ_0 the tangential parameter, $d_0(\xi)$ the distance between the boundary of obstacle and current position ξ, and $\bar{\varepsilon}$ a small positive threshold of the saturation function τ.

Fig. 3 illustrates the normal vector $\boldsymbol{n}(\xi)$ and tangential vector $\boldsymbol{t}(\xi)$ of point ξ in the presence of a sphere obstacle. As is seen, a tangential plane can be constructed on the of the outer sphere surface, i.e., $F(\xi)\geqslant 1$. It is obvious that $\boldsymbol{n}(\xi)$ is perpendicular to the tangential plane and outward from the obstacle, while $\boldsymbol{t}(\xi)$ is a horizontal vector on the tangential plane.

Then the disturbed fluid velocity $\bar{\boldsymbol{v}}(\xi)$ can be calculated by

$$\bar{\boldsymbol{v}}(\xi)=\boldsymbol{P}(\xi)\boldsymbol{v}(\xi) \tag{9}$$

Sometimes the adaption of $\|\bar{\boldsymbol{v}}(\xi)\|$ is required to ensure the planned path to be tracked more easily. Then, waypoints along time can be computed by integrating $\bar{\boldsymbol{v}}(\xi)$ recursively:

$$\{\xi\}_{t+1}=\{\xi\}_t+\bar{\boldsymbol{v}}(\xi)\Delta t \tag{10}$$

where $\{\xi\}_t$ and $\{\xi\}_{t+1}$ are the current and next waypoint respectively, Δt the iteration time step. Eventually we can obtain all the planned waypoints, forming the modified streamline, i.e., the planned path.

The characters of the planned path are as follows:

(1) The path can avoid obstacle safely.

Proof. Vectors $\boldsymbol{n}(\xi)$ and $\boldsymbol{t}(\xi)$ are perpendicular exactly, i.e., $\boldsymbol{n}(\xi)^{\mathrm{T}}\boldsymbol{t}(\xi)=0$. Suppose that point ξ is on the boundary of the obstacle, i.e., $F(\xi)=1$, then $\boldsymbol{P}(\xi)$ is simplified as

$$\boldsymbol{P}(\xi)=\boldsymbol{I}-\frac{\boldsymbol{n}(\xi)\boldsymbol{n}(\xi)^{\mathrm{T}}}{\boldsymbol{n}(\xi)^{\mathrm{T}}\boldsymbol{n}(\xi)}+\frac{\tau\boldsymbol{t}(\xi)\boldsymbol{n}(\xi)^{\mathrm{T}}}{\|\boldsymbol{t}(\xi)\|\|\boldsymbol{n}(\xi)\|}$$

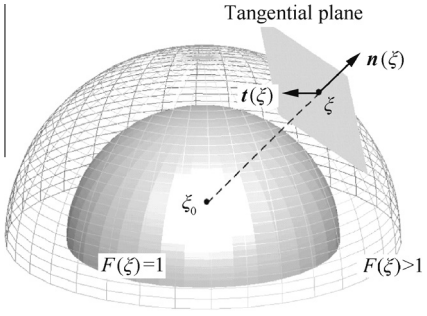

Fig. 3 Illustration of normal and tangential vector.

Therefore, we can infer

$$\begin{aligned}\boldsymbol{n}(\xi)^{\mathrm{T}}\bar{\boldsymbol{v}}(\xi)&=\boldsymbol{n}(\xi)^{\mathrm{T}}\boldsymbol{P}(\xi)\boldsymbol{v}(\xi)\\&=\left(\boldsymbol{n}(\xi)^{\mathrm{T}}-\boldsymbol{n}(\xi)^{\mathrm{T}}+\frac{\tau\boldsymbol{n}(\xi)^{\mathrm{T}}\boldsymbol{t}(\xi)\boldsymbol{n}(\xi)^{\mathrm{T}}}{\|\boldsymbol{t}(\xi)\|\|\boldsymbol{n}(\xi)\|}\right)\boldsymbol{v}(\xi)=0\end{aligned}$$

The equation $\boldsymbol{n}(\xi)^{\mathrm{T}}\bar{\boldsymbol{v}}(\xi)=0$ means that the normal component of $\bar{\boldsymbol{v}}(\xi)$ is 0, so the path will not penetrate into obstacle. □

(2) The path can reach the destination eventually.

Proof. From Eq. (2), the original flow velocity $\boldsymbol{v}(\xi)$ always points to destination. Therefore, if velocity $\bar{\boldsymbol{v}}(\xi)$ satisfies $\boldsymbol{v}(\xi)^{\mathrm{T}}\bar{\boldsymbol{v}}(\xi)\geqslant 0$, the planned path will converge to the target point. Besides, $\bar{\boldsymbol{v}}(\xi)\approx\boldsymbol{v}(\xi)$ should be satisfied if point ξ is near to ξ_{d}.

$$\begin{aligned}\boldsymbol{v}(\xi)^{\mathrm{T}}\bar{\boldsymbol{v}}(\xi)=\boldsymbol{v}(\xi)^{\mathrm{T}}\boldsymbol{P}(\xi)\boldsymbol{v}(\xi)&=\|\boldsymbol{v}(\xi)\|^2\left(1-\frac{\cos^2\langle\boldsymbol{v}(\xi),\boldsymbol{n}(\xi)\rangle}{|F(\xi)|^{\frac{1}{\rho(\xi)}}}\right)\\&+\frac{\tau\boldsymbol{v}(\xi)^{\mathrm{T}}\boldsymbol{t}(\xi)\boldsymbol{n}(\xi)^{\mathrm{T}}\boldsymbol{v}(\xi)}{|F(\xi)|^{\frac{1}{\sigma(\xi)}}\|\boldsymbol{t}(\xi)\|\|\boldsymbol{n}(\xi)\|}\end{aligned}$$

As $F(\xi)\geqslant 1$ and $\cos^2\langle\boldsymbol{v}(\xi),\boldsymbol{n}(\xi)\rangle\leqslant 1$ hold, we infer $1-\cos^2\langle\boldsymbol{v}(\xi),\boldsymbol{n}(\xi)\rangle/|F(\xi)|^{\frac{1}{\rho(\xi)}}\geqslant 0$, where $\langle\boldsymbol{v}(\xi),\boldsymbol{n}(\xi)\rangle$ denotes the angle between $\boldsymbol{v}(\xi)$ and $\boldsymbol{n}(\xi)$. From Eq. (8), we infer $\tau\boldsymbol{v}(\xi)^{\mathrm{T}}\boldsymbol{t}(\xi)\boldsymbol{n}(\xi)^{\mathrm{T}}\boldsymbol{v}(\xi)\geqslant 0$. Therefore, $\boldsymbol{v}(\xi)^{\mathrm{T}}\bar{\boldsymbol{v}}(\xi)\geqslant 0$ holds.

When $\xi\approx\xi_{\mathrm{d}}$, i.e., $d(\xi)\to 0$, thus $\rho(\xi)\to 0$ and $\sigma(\xi)\to 0$, thus $|F(\xi)|^{\frac{1}{\rho(\xi)}}\to\infty$ and $|F(\xi)|^{\frac{1}{\sigma(\xi)}}\to\infty$, thus $\boldsymbol{P}(\xi)\to\boldsymbol{I}$. Therefore $\bar{\boldsymbol{v}}(\xi)\approx\boldsymbol{v}(\xi)$ holds. □

(3) The path follows the shape of obstacle efficiently.

Proof. When UAV is moving towards but still far from the obstacle, $F(\xi)\to\infty$, then $\bar{\boldsymbol{v}}(\xi)\approx\boldsymbol{v}(\xi)$, so it moves along the original straight streamline. When UAV gets closer to the obstacle, i.e., $\boldsymbol{n}(\xi)^{\mathrm{T}}\boldsymbol{v}(\xi)<0$, its motion converges to the direction of the tangent. When UAV is moving away from the obstacle, i.e., $\boldsymbol{n}(\xi)^{\mathrm{T}}\boldsymbol{v}(\xi)>0$, velocity component of $\bar{\boldsymbol{v}}(\xi)$ points into the obstacle, which makes the path follow the shape of obstacle well and converge to the original streamline swiftly. Therefore, the planned path meets the requirements of terrain following in true battlefield.

However, sometimes it is undesired to follow the shape of obstacle after UAV passes the obstacle, so the repulsive and tangential velocity can be ignored when UAV moves away from the obstacle. We define $\mathrm{sf}\in\{0,1\}$ as the shape-following parameter: sf = 1 if the feature of shape-following is demanded; sf = 0 on the other hand. Then the perturbation matrix $\boldsymbol{P}(\xi)$ is redefined as follows:

$$\boldsymbol{P}(\xi)=\begin{cases}\boldsymbol{I}-\dfrac{\boldsymbol{n}(\xi)\boldsymbol{n}(\xi)^{\mathrm{T}}}{|F(\xi)|^{\frac{1}{\rho(\xi)}}\boldsymbol{n}(\xi)^{\mathrm{T}}\boldsymbol{n}(\xi)}+\dfrac{\tau\boldsymbol{t}(\xi)\boldsymbol{n}(\xi)^{\mathrm{T}}}{|F(\xi)|^{\frac{1}{\sigma(\xi)}}\|\boldsymbol{t}(\xi)\|\|\boldsymbol{n}(\xi)\|} & \boldsymbol{n}(\xi)^{\mathrm{T}}\boldsymbol{v}(\xi)<0\text{ or }\mathrm{sf}=1\\ \boldsymbol{I} & \boldsymbol{n}(\xi)^{\mathrm{T}}\boldsymbol{v}(\xi)\geqslant 0\text{ and }\mathrm{sf}=0\end{cases} \tag{11}$$

Fig. 4(a) illustrates the shape-following path from the start point $\xi_s = (0, 0, 0.5)$ to the target point $\xi_d = (10, 0, 0.5)$ with $sf = 1$. As is seen, the whole path follows the shape of obstacle well and converges to the original streamline swiftly. Fig. 4(b) illustrates the not-shape-following path with $sf = 0$ and the path goes straight to the target after it passes the obstacle. □

3.2. Analysis of disturbed fluid velocity

The modified velocity $\bar{\boldsymbol{v}}(\xi)$ defined by Eq. (9) can be expressed as

$$\bar{\boldsymbol{v}}(\xi) = \boldsymbol{P}(\xi)\boldsymbol{v}(\xi) = \boldsymbol{v}(\xi) - \frac{\boldsymbol{n}(\xi)^{\mathrm{T}}\boldsymbol{v}(\xi)}{|F(\xi)|^{\frac{1}{\rho(\xi)}}\boldsymbol{n}(\xi)^{\mathrm{T}}\boldsymbol{n}(\xi)}\boldsymbol{n}(\xi) + \frac{\tau\boldsymbol{n}(\xi)^{\mathrm{T}}\boldsymbol{v}(\xi)}{|F(\xi)|^{\frac{1}{\sigma(\xi)}}\|\boldsymbol{t}(\xi)\|\|\boldsymbol{n}(\xi)\|}\boldsymbol{t}(\xi)$$

As is seen, $\bar{\boldsymbol{v}}(\xi)$ consists three parts: $\boldsymbol{v}(\xi)$ can be called the attractive velocity, whose magnitude is the constant C; $-\frac{\boldsymbol{n}(\xi)^{\mathrm{T}}\boldsymbol{v}(\xi)}{|F(\xi)|^{\frac{1}{\rho(\xi)}}\boldsymbol{n}(\xi)^{\mathrm{T}}\boldsymbol{n}(\xi)}\boldsymbol{n}(\xi)$ is taken as the repulsive velocity; $\frac{\tau\boldsymbol{n}(\xi)^{\mathrm{T}}\boldsymbol{v}(\xi)}{|F(\xi)|^{\frac{1}{\sigma(\xi)}}\|\boldsymbol{t}(\xi)\|\|\boldsymbol{n}(\xi)\|}\boldsymbol{t}(\xi)$ can be called the tangential velocity. Similarly, the perturbation matrix $\boldsymbol{P}(\xi)$ can be divided into three parts: attractive matrix $\boldsymbol{I}$, repulsive matrix $-\frac{\boldsymbol{n}(\xi)\boldsymbol{n}(\xi)^{\mathrm{T}}}{|F(\xi)|^{\frac{1}{\rho(\xi)}}\boldsymbol{n}(\xi)^{\mathrm{T}}\boldsymbol{n}(\xi)}$ and tangential matrix $\frac{\tau\boldsymbol{t}(\xi)\boldsymbol{n}(\xi)^{\mathrm{T}}}{|F(\xi)|^{\frac{1}{\sigma(\xi)}}\|\boldsymbol{t}(\xi)\|\|\boldsymbol{n}(\xi)\|}$. It can be analyzed that the magnitudes of repulsive and tangential velocities increase with ρ_0 and σ_0 respectively. Therefore, we can readjust the shape of the path by changing parameters ρ_0 or σ_0.

This method is similar to the virtual force method or the artificial potential field method to some degree. However, the perturbation matrix by this method can describe the effect of obstacles on path more objectively, considering the shape of obstacles and the position of UAV.

Besides, compared with IFDS,[23] the tangential matrix is first introduced into the perturbation matrix, therefore feasible paths can easily be obtained in 3-D environment. The velocity by IFDS can only be divided into two parts: the attractive velocity and the repulsive velocity. The corresponding paths with different repulsive parameters can be obtained. However, the distribution of these paths is limited. Fig. 5 illustrates the case that UAV avoids a sphere obstacle by IFDS without considering tangential velocity, of which the repulsive parameter ρ_0 can be 0.1, 1, 2, 5, 10. As depicted in Fig. 5(a), the lager ρ_0 is, the earlier the path deflects on the vertical plane. However, there is no deflection on the horizontal plane (seen in Fig. 5(b)). As a result, the planned paths may be unfeasible for UAVs with poor longitudinal maneuvering capability. Fig. 6

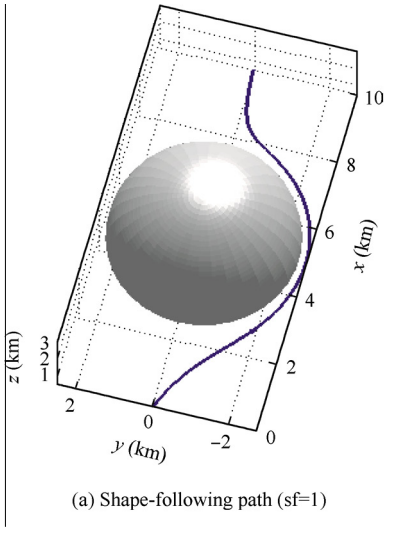

(a) Shape-following path (sf=1)

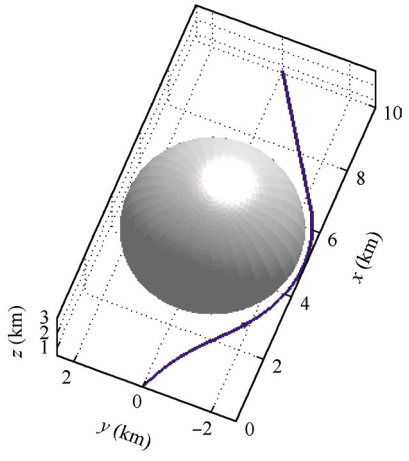

(b) Not-shape-following path (sf=0)

Fig. 4 Control of shape-following or not-shape-following property.

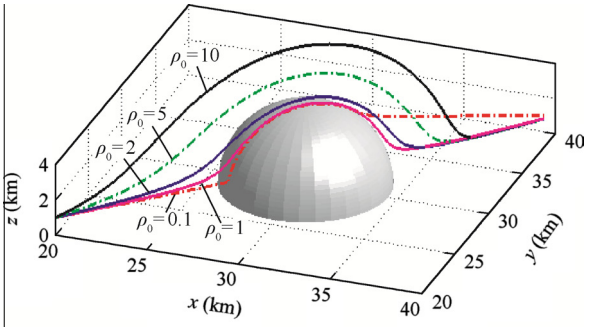

(a) 3-D paths with different parameters

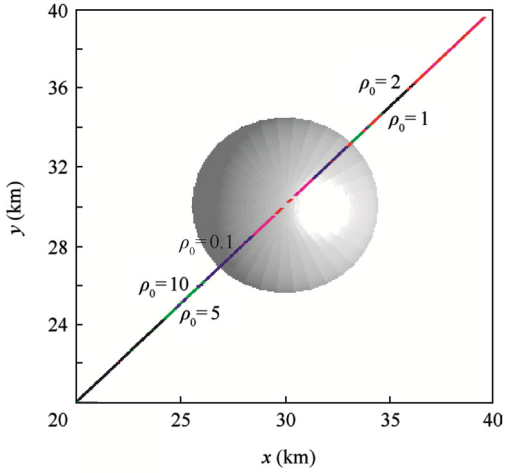

(b) Paths in *x*-*y* plane

Fig. 5 Planned paths without considering tangential velocity.

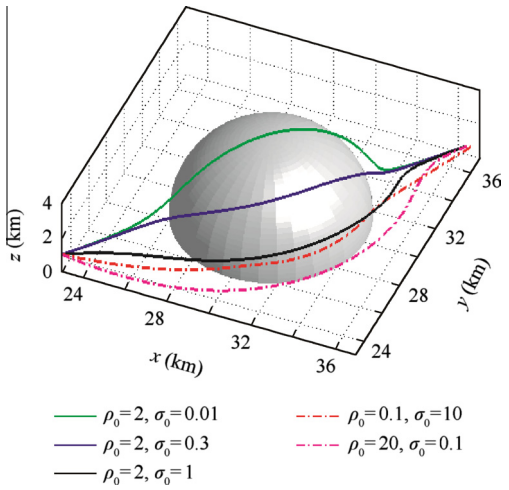

Fig. 6 Planned paths considering tangential velocity.

shows the path by the proposed method, where the tangential velocity is introduced into the modified velocity in this paper. The adaption to repulsive and tangential parameter makes it much easier to tune the path to obtain a feasible path. It is evident that more optional paths are gained by adapting ρ_0 or σ_0, and the paths can deflect on the vertical and horizontal plane at the same time.

3.3. Path planning for obstacle with sharp edges

The planned path can follow the shape of obstacle well. When there is an obstacle with sharp edges, e.g., cuboid, the planned path would be unfeasible as sharp turns exist. To solve this problem, the obstacle should be replaced by an object with a smooth convex envelope that tightly encloses the obstacle.[30] In this paper, parameters a, b, c, d, e and f are adjusted to obtain this object. A cuboid convex $(d>1, e>1, f>1)$ is taken as an example. Through analysis, the larger d, e, f are, the sharper edges the obstacle has. Therefore, any too large parameter d, e, f should decrease to some extent to smooth the surface. At the same time, axis parameters a, b, c should increase to ensure that the new defined object can fit around the original obstacle tightly.

Suppose a cuboid with sharp edges defined as $\left(\frac{x-10}{5}\right)^{40}+\left(\frac{y}{3}\right)^{40}+\left(\frac{z}{8}\right)^{40}=1$ is constructed in the planning space. Fig. 7(a) shows the planned path, which is obviously unfeasible. In Fig. 7(b), the equation of obstacle is redefined to be $\left(\frac{x-10}{6}\right)^{4}+\left(\frac{y}{4}\right)^{4}+\left(\frac{z}{9}\right)^{4}=1$ and the original cuboid is enclosed by the new one, and the subsequently planned path is much smoother.

4. Path planning for multiple obstacles

4.1. Path planning for non-overlapping obstacles

Suppose there are K non-overlapping obstacles in flight environment. The kth $(k=1,2,\ldots,K)$ obstacle centers at $\xi_{0,k}=(x_{0,k},y_{0,k},z_{0,k})$ with parameters a_k, b_k, c_k, d_k, e_k, f_k. For the kth obstacle, the definitions of obstacle equation $F_k(\xi)=1$, the repulsive parameter $\rho_{0,k}$, the tangential parameter $\sigma_{0,k}$, the normal vector $\boldsymbol{n}_k(\xi)$, the tangential vector $\boldsymbol{t}_k(\xi)$, the

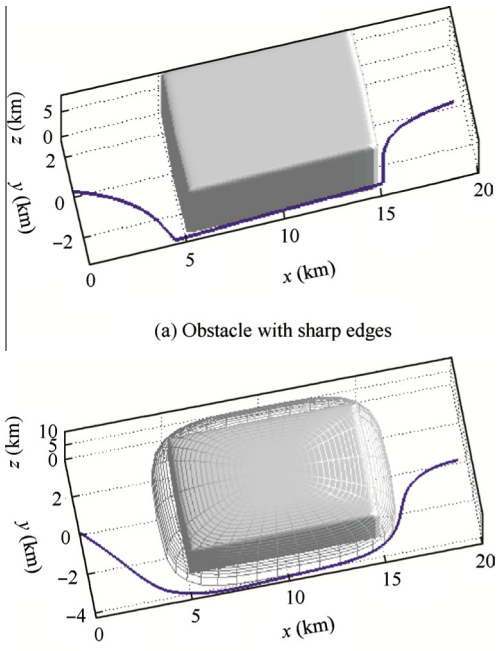

Fig. 7 Adjustment of obstacle with sharp edges.

tangent-orientation parameter τ_k, $\rho_k(\xi)$, $\sigma_k(\xi)$ and the shape-following parameter $\mathrm{sf}_k\in\{0,1\}$ are the same as in Section 3.1. Then the perturbation matrix of the kth obstacle $\boldsymbol{P}_k(\xi)$ can be determined, which is the same as Eq. (11).

The weighting coefficient of the kth obstacle is defined as

$$\omega_k(\xi)=\prod_{i=1,i\neq k}^{K}\frac{F_i(\xi)-1}{(F_k(\xi)-1)+(F_i(\xi)-1)} \tag{12}$$

As $\sum_{i=1}^{K}\omega_i(\xi)\leqslant 1$ holds, $\tilde{\omega}_k(\xi)$ is defined as the relative weighting coefficient by normalization processing:

$$\tilde{\omega}_k(\xi)=\frac{\omega_k(\xi)}{\sum_{i=1}^{K}\omega_i(\xi)} \tag{13}$$

The overall perturbation matrix $\boldsymbol{P}(\xi)$ is given by

$$\boldsymbol{P}(\xi)=\sum_{k=1}^{K}\tilde{\omega}_k(\xi)\boldsymbol{P}_k(\xi) \tag{14}$$

The characters of the planned path are as follows:

(1) The path can avoid all the obstacles safely.

Proof. Suppose ξ is on the boundary of the kth obstacle, i.e., $F_k(\xi)=1$, then $\omega_k(\xi)=1$, $\omega_i(\xi)=0$, thus $\tilde{\omega}_k(\xi)=1$, $\tilde{\omega}_i(\xi)=0$ $(i=1,2,\ldots,K$ and $i\neq k)$. Hence the equation $\boldsymbol{P}(\xi)=\boldsymbol{P}_k(\xi)$ holds, meaning that the remaining proof is the same as that of path planning for one obstacle in Section 3.1. □

(2) The path can reach the destination eventually.

Proof. For the kth obstacle, the equation $\boldsymbol{v}(\xi)^{\mathrm{T}}\boldsymbol{P}_k(\xi)\boldsymbol{v}(\xi)\geqslant 0$ holds. From Eqs. (12) and (13), we get $0\leqslant\tilde{\omega}_k(\xi)\leqslant 1$. Therefore, $\boldsymbol{v}(\xi)^{\mathrm{T}}\bar{\boldsymbol{v}}(\xi)=\sum_{k=1}^{K}\tilde{\omega}_k(\xi)\boldsymbol{v}(\xi)^{\mathrm{T}}\boldsymbol{P}_k(\xi)\boldsymbol{v}(\xi)\geqslant 0$ holds.

If $\xi \approx \xi_d$, $\boldsymbol{P}_k(\xi) \to \boldsymbol{I}$ $(k = 1, 2, \ldots, K)$. Therefore, $\boldsymbol{P}(\xi) \to \boldsymbol{I}$ holds, thus $\bar{\boldsymbol{v}}(\xi) \approx \boldsymbol{v}(\xi)$. □

(3) When the path is near to any obstacle, it can follow the shape of this obstacle efficiently.

Proof. Suppose ξ is near to the kth obstacle, then $\tilde{\omega}_k(\xi) \to 1$, $\tilde{\omega}_i(\xi) \to 0$ $(i = 1, 2, \ldots, K$ and $i \neq k)$, thus $\boldsymbol{P}(\xi) \approx \boldsymbol{P}_k(\xi)$ holds. Then the remaining proof is the same as that of path planning for one obstacle in Section 3.1. □

4.2. Path planning for overlapping obstacles

Suppose there are two overlapping obstacles centering at O_i and O_{i+1}. The concave region produced by the two obstacles is called trap area (TA), shown as the dash area in Fig. 8, with ξ'_d the chosen virtual target, which will be discussed later. If velocity $\bar{\boldsymbol{v}}(\xi)$ points to TA, UAV may fall into the trap area. Eventually, UAV will arrive at the intersection of the two obstacles, leading to the failure of calculation.

To solve the above-mentioned problem, the method of virtual target is applied when the following three criteria are satisfied:

(1) In the planning space, there are overlapping obstacles with centers $O_i, O_{i+1}, \ldots, O_j$.
(2) The velocity $\bar{\boldsymbol{v}}(\xi)$ points to TA.
(3) $\min\{d(\xi, O_i), d(\xi, O_{i+1}), \ldots, d(\xi, O_j)\} \leqslant d_{TA}$.

where $d(\xi, O_i)$ denotes the distance between ξ and obstacle center O_i, in order to determine the proper time to choose virtual target; d_{TA} is defined as the detecting distance of TA and it is positively correlated to the quantity of overlapping obstacles and their sizes.

Once the trap area is detected, a portion of spherical surface called A_v is established, where the optimal virtual target will be chosen. The radius of A_v is d_{TA}; the horizontal span angle ϕ_v satisfies $\phi - \phi_m \leqslant \phi_v \leqslant \phi + \phi_m$; the vertical span angle μ_v satisfies $-\mu_m \leqslant \mu_v \leqslant \mu_m$. Angle ϕ_m and μ_m are the maximum turning angle and flight-path angle of UAV respectively and the turning angle ϕ is defined as

$$\phi = \arctan\left(\frac{v_y}{v_x}\right) \tag{15}$$

where $\boldsymbol{v} = [v_x, v_y, v_z]^T$ is the initial fluid velocity at the moment.

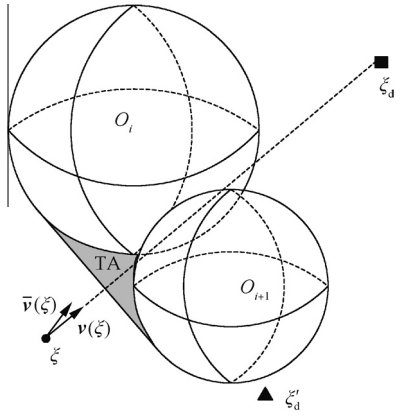

Fig. 8 Illustration of trap area.

The spherical surface A_v can be discretized equally into N_1 points in vertical direction and N_2 points in horizontal direction, thus generating N_1N_2 points. And the optimal virtual target is then chosen from these points. Fig. 9 shows the methodology of generating virtual targets. It displays the virtual sphere area A_v with radius d_{TA}, and any optional virtual target ξ_v is shown as a black spot. θ_1 is the angle between $\xi\xi_d$ and $\xi\xi_v$, and θ_2 is the angle between $\xi\xi_v$ and $\xi_v\xi_d$.

Inspired by the method of choosing sub-goal,[31] we define J as the heuristic function of any point ξ_v from the area A_v:

$$J = \lambda_1 S + \lambda_2 D + \lambda_3 M + \lambda_4 G \tag{16}$$

where S is the cost of flying safety, D the cost of distance, M the cost of target switch, G the cost of TA, and λ_1, λ_2, λ_3, λ_4 are the weighs of each cost. And we have

$$S = \begin{cases} \sum_{i=1}^{K} 1/F_i(\xi_v) & \text{If } F_i(\xi_v) > 1, \quad \forall i = 1, 2, \ldots, K \\ +\infty & \text{Otherwise} \end{cases} \tag{17}$$

$$D = \frac{d(\xi_v, \xi_d) - \min d(\xi_v, \xi_d)}{\max d(\xi_v, \xi_d) - \min d(\xi_v, \xi_d)} \tag{18}$$

$$M = \lambda_{\theta_1} \frac{\theta_1 - \min \theta_1}{\max \theta_1 - \min \theta_1} + \lambda_{\theta_2} \frac{\theta_2 - \min \theta_2}{\max \theta_2 - \min \theta_2} \tag{19}$$

$$G = \begin{cases} 0 & \text{If } \xi\xi_v \cap \text{TA} = \varnothing \\ +\infty & \text{Otherwise} \end{cases} \tag{20}$$

where $d(\xi_v, \xi_d)$ is the distance between ξ_v and ξ_d, and $\lambda_{\theta 1}$, $\lambda_{\theta 2}$ the weights of θ_1 and θ_2 respectively.

Then the virtual target ξ'_d is selected as

$$\xi'_d = \arg\ \min\ J \tag{21}$$

The virtual target ξ'_d can instruct the vehicle to avoid the trap area. When UAV arrives at ξ'_d successfully, the target point is reverted to ξ_d.

5. Trajectory propagation

5.1. Analysis of feasibility of planned path

To judge the feasibility of the planned path, the method called trajectory propagation[26,27] is adopted here. For a flyable path, the corresponding state variables of UAV, especially the

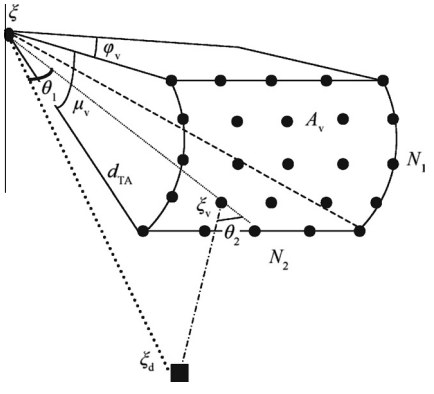

Fig. 9 Methodology of generating virtual targets.

dynamic pressure, should match on the connection of each path segment. Besides, these variables should be continuous and within their ranges respectively. Trajectory propagation method is the process of solving the vehicle dynamic differential equations by iteration with the constraints of the planned path and UAV dynamics. State variables and guidance command can be obtained eventually.

The independent variable of UAV dynamic equations is usually time t. However, it is replaced by the forward distance x_g in this paper. The advantage is that the relation between the planned path and the kinematics and dynamics equations can be more distinct, and the state variables can be obtained more easily. Besides, UAV velocity can be replaced by dynamic pressure in order to simplify the analysis, as dynamic pressure is directly related to velocity and altitude.

First, the earth-surface inertial reference frame o-$x_g y_g z_g$ is established for convenience. It could be obtained by converting the coordinate system o-xyz defined in Section 2.1. Therefore, any planned waypoint $\xi = (x, y, z)$ in o-xyz can be transformed into $\xi_g = (x_g, y_g, z_g)$ in o-$x_g y_g z_g$:

$$\begin{cases} x_g = x\cos\theta_{sd} + y\sin\theta_{sd} \\ y_g = -(-x\sin\theta_{sd} + y\cos\theta_{sd}) \\ z_g = -z \end{cases} \tag{22}$$

where $\theta_{sd} = \arctan(y_d - x_d/(y_s - x_s))$ denotes the angle between $\xi_s\xi_d$ and x axis of o-xyz, x_g the forward distance, y_g the offside distance and z_g the vertical distance.

Suppose there are N waypoints and $N-1$ path segments of the planned path. Take the nth path segment as an example. The initial point is $\xi_{gn} = (x_{gn}, y_{gn}, z_{gn})$; the final point is $\xi_{g(n+1)} = \left(x_{g(n+1)}, y_{g(n+1)}, z_{g(n+1)}\right)$; the initial and final velocity are V_n and V_{n+1} respectively. Then by the cubic spline curve fitting method, the expressions of altitude $h(h = -z_g)$, offside distance y_g and velocity V can be obtained as follows:

$$\begin{cases} h(x_g) = a_3\bar{x}^3 + a_2\bar{x}^2 + a_1\bar{x} + a_0 \\ y_g(x_g) = b_3\bar{x}^3 + b_2\bar{x}^2 + b_1\bar{x} + b_0 \\ V(x_g) = c_3\bar{x}^3 + c_2\bar{x}^2 + c_1\bar{x} + c_0 \end{cases} \tag{23}$$

where a_i, b_i, c_i $(i = 0, 1, 2, 3)$ are the corresponding parameters, and $\bar{x} = x_g - x_{gn}$.

Suppose the attitude control loop of UAV is stable, then a three-degree-of-freedom (3-DOF) point-mass model is given detailedly as follows:

$$\begin{cases} \dot{x}_g = V\cos\mu\cos\varphi \\ \dot{y}_g = V\cos\mu\sin\varphi \\ \dot{h} = V\sin\mu \\ \dot{V} = (T\cos\alpha\cos\beta - D - mg\sin\mu)/m \\ \dot{\mu} = \frac{1}{mV}[T(\sin\alpha\cos\gamma + \cos\alpha\sin\beta\sin\gamma) + L\cos\gamma - Y\sin\gamma - mg\cos\mu] \\ \dot{\varphi} = \frac{1}{mV\cos\mu}[T(\sin\alpha\sin\gamma - \cos\alpha\sin\beta\cos\gamma) + L\sin\gamma + Y\cos\gamma] \end{cases} \tag{24}$$

where μ is the flight-path angle, φ the heading angle, α the angle of attack, β the sideslip angle, γ the bank angle, $h = -z_g$ the altitude, V the inertial velocity, T the engine thrust, m the mass of vehicle, $D = C_D\rho V^2 S_w/2$ the air drag force, $L = C_L\rho V^2 S_w/2$ the lift force, $Y = C_Y\rho V^2 S_w/2$ the side force, with S_w the wing area, ρ the air density and C_D, C_L and C_Y are corresponding aerodynamic coefficients.

In order to simplify the kinetic model, coordinated turn is the main turn mode in this paper. Hence, β is ignored, i.e., $\beta \approx 0°$. As a result, side force Y can also be ignored. Besides, components $T(\sin\alpha\cos\gamma + \cos\alpha\sin\beta\sin\gamma)$ and $T(\sin\alpha\sin\gamma - \cos\alpha\sin\beta\cos\gamma)$ can be neglected since the angle of attack α is small. Besides, we transform the independent variable of Eq. (24) from t to x_g. Therefore, the simplified UAV model is given by

$$\begin{cases} \dot{h}(x_g) = \dfrac{\tan\mu}{\cos\varphi} \\ \dot{y}_g(x_g) = \tan\varphi \\ \dot{\mu}(x_g) = \dfrac{L\cos\gamma - mg\cos\mu}{mV^2\cos\mu\cos\varphi} \\ \dot{\varphi}(x_g) = \dfrac{L\sin\gamma}{mV^2\cos^2\mu\cos\varphi} \\ \dot{V}(x_g) = \dfrac{T\cos\alpha - D - mg\sin\mu}{mV\cos\mu\cos\varphi} \end{cases} \tag{25}$$

From Eq. (23), the heading angle φ, the flight-path angle μ and their respective derivatives with respect to x_g can be calculated as follows:

$$\varphi = \arctan(\dot{y}_g(x_g)) = \arctan\left(3b_3\bar{x}^2 + 2b_2\bar{x} + b_1\right) \tag{26}$$

$$\dot{\varphi}(x_g) = \frac{\partial\varphi}{\partial x_g} = \frac{6b_3\bar{x} + 2b_2}{1 + (3b_3\bar{x}^2 + 2b_2\bar{x} + b_1)^2} \tag{27}$$

$$\mu = \arctan\left(\dot{h}(x_g)\cos\varphi\right) = \arctan[(3a_3\bar{x}^2 + 2a_2\bar{x} + a_1)\cos\varphi] \tag{28}$$

$$\dot{\mu}(x_g) = \frac{\partial\mu}{\partial x_g} = \frac{(6a_3\bar{x} + 2a_2)\cos\varphi - (3a_3\bar{x}^2 + 2a_2\bar{x} + a_1)\sin\varphi\dot{\varphi}(x_g)}{1 + [(3a_3\bar{x}^2 + 2a_2\bar{x} + a_1)\cos\varphi]^2} \tag{29}$$

Substituting $L = C_L\rho V^2 S_w/2$ and $Q = \rho V^2/2$ into the third equation of Eq. (25) yields

$$Q = \frac{mg\rho\cos\mu}{\rho S_w C_L\cos\gamma - 2m\dot{\mu}(x_g)\cos\mu\cos\varphi} \tag{30}$$

From the third and the fourth equation of Eq. (25), the bank angle can be inferred:

$$\gamma = \arctan\left(\frac{\dot{\varphi}(x_g)\cos\mu}{\dot{\mu}(x_g) + \frac{\rho g}{2Q\cos\varphi}}\right) \tag{31}$$

From the fifth equation of Eq. (25), we compute the engine thrust:

$$T = mV\cos\mu\cos\varphi(3c_3\bar{x}^2 + 2c_2\bar{x} + c_1) + C_D S_w Q + mg \times \sin\mu \tag{32}$$

Substituting the first and fifth equation of Eq. (25) into the differentiation of $Q = \rho V^2/2$ yields

$$\dot{Q}(x_g) = \left(\frac{Q}{\rho}\frac{\partial\rho}{\partial h} - \rho g\right)\frac{\tan\mu}{\cos\varphi} + \frac{\rho T\cos\alpha - \rho C_D Q S_w}{m\cos\mu\cos\varphi} \tag{33}$$

where $\partial\rho/\partial h$ is a known function we can get from the air data.

In addition, the initial and final constraints of the nth path segment are

$$\begin{cases} h_{init} = -z_{gn}, \quad x_{g-init} = x_{gn}, \quad y_{g-init} = y_{gn} \\ V_{init} = V_n, \quad Q_{init} = \rho V_n^2/2 \\ h_{final} = -z_{g(n+1)}, \quad x_{g-final} = x_{g(n+1)}, \quad y_{g-final} = y_{g(n+1)} \\ V_{final} = V_{n+1}, \quad Q_{final} = \rho V_{n+1}^2/2 \end{cases} \tag{34}$$

where h_{init}, $x_{\text{g-init}}$, $y_{\text{g-init}}$, V_{init} and Q_{init} are the initial altitude, forward distance, offside distance, velocity and dynamic pressure respectively; h_{final}, $x_{\text{g-final}}$, $y_{\text{g-final}}$, V_{final} and Q_{final} denote the corresponding final constraints.

The procedure of trajectory propagation is shown in Fig. 10. First we acquire the cubic curve expressions, the initial and final constraints of path segment; the initial values of α and T, i.e., α_{init} and T_{init}, are computed by the trim of initial point. For current forward distance x_g, the variables φ, $\dot{\varphi}(x_g)$, μ and $\dot{\mu}(x_g)$ are calculated from Eqs. (26)–(29); α is guessed as $\alpha(x_g)$ and then C_L, C_D, γ, $\dot{Q}$ would be computed. Then, estimates of two types of dynamic pressure are obtained: Q_{diff} is calculated from the differential equation of Eq. (33); Q_{alg} can be obtained directly by the algebraic approach of Eq. (30). Then, Q_{diff} and Q_{alg} are compared to determine whether they are consistent (i.e., $|Q_{\text{alg}} - Q_{\text{diff}}| \leqslant \varepsilon$, where ε is a small positive number). If not, $\alpha(x_g)$ is adjusted until Q_{diff} and Q_{alg} match. The above steps continue by iteration (where Δx_g is the integration step: $x_g = x_g + \Delta x_g$) until the final point of this path segment. Then, terminal dynamic pressure Q_{final} and computational dynamic pressure Q_{diff} of the final point are compared to judge whether they are consistent (i.e., $|Q_{\text{diff}} - Q_{\text{final}}| \leqslant \varepsilon'$, where ε' is a small positive number). If Q_{final} and Q_{diff} do not match or other state variables are out of their respective ranges, the path is unfeasible and therefore ρ_0 and σ_0 of path planning should be adapted, described detailedly in Section 5.2. Otherwise, the abovementioned process repeats for the next path segment until the destination. The path is feasible only if all path segments have judged to be flyable.

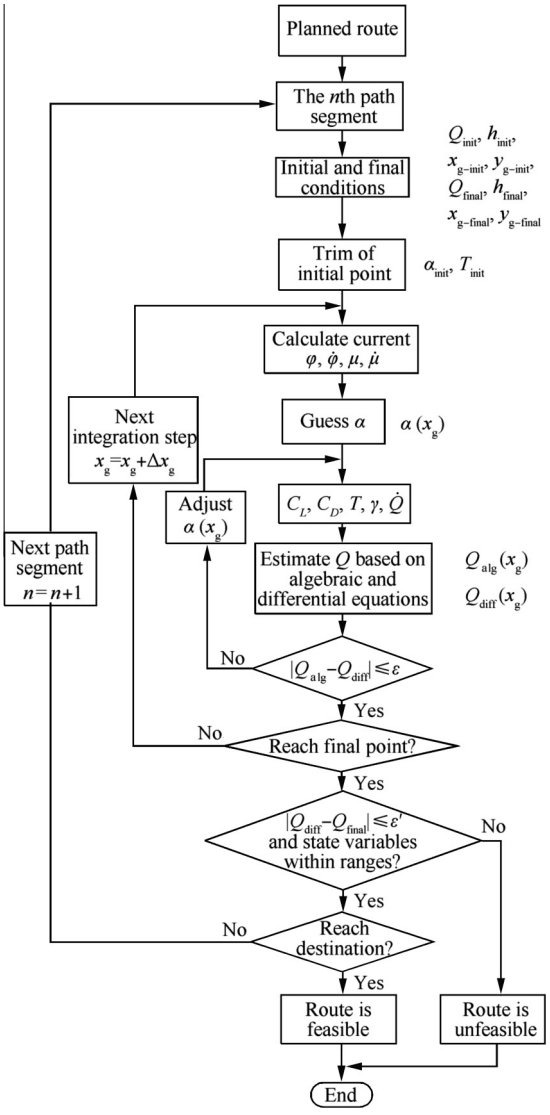

Fig. 10 Procedure of trajectory propagation.

5.2. Strategy of adjusting repulsive and tangential parameters

If the path is unfeasible judged by the trajectory propagation, the repulsive or tangential parameters should be adjusted by some strategies until a feasible one is obtained.

According to Eq. (14), the overall interfered fluid field is calculated by the superposition of all component ones, any of which is only influenced by one obstacle with the proportion $\tilde{\omega}_k(\xi)$. According to Eqs. (12) and (13), the nearer to an obstacle UAV is, i.e., the closer to 1 the function $F(\xi)$ is, the bigger the proportion $\tilde{\omega}_k(\xi)$ of the obstacle. Therefore, the flow is mainly influenced by those obstacles near to UAV (i.e., $\tilde{\omega}_k(\xi) \geqslant w$, where w is the criteria).

According to Section 3.2, the shape of streamline, i.e., the planned path can be changed by adjusting different parameters of obstacles, as the repulsive velocity and tangential velocity are positively correlated to the repulsive parameter ρ_0 and tangential parameter σ_0 respectively. Besides, there is always no vertical component in tangential velocity while vertical component usually exists in repulsive velocity. Therefore, the larger ρ_0, the more vertical component of velocity $\bar{\boldsymbol{v}}(\xi)$; the larger σ_0, the more horizontal component of $\bar{\boldsymbol{v}}(\xi)$.

On the basis of the above analysis, when the unflyable path segment is confirmed by the trajectory propagation, parameters of obstacles, especially those close to this path segment should be adjusted. The resolved variables of the planned path can offer a reference for modifying repulsive or tangential parameters adaptively when necessary. And the situation of avoiding a sphere obstacle is discussed here. If the resolved state variables e.g., the flight-path angle μ is out of range $\mu_{\max}$, the vertical component of $\bar{\boldsymbol{v}}(\xi)$ may be too large. Therefore, σ_0 should increase or ρ_0 should decrease, and there is a positive correlation adaptively between the adjustment of parameters and the state variable error, e.g., $|\mu - \mu_{\max}|$. On the other hand, if the resolved variable, e.g., the bank angle γ is out of range, the horizontal component of $\bar{\boldsymbol{v}}(\xi)$ is too large. Hence the tangential velocity should decrease by decreasing σ_0 or increasing ρ_0 adaptively. The procedure of adjusting repulsive and tangential parameters is shown in Fig. 11.

6. Simulation

In order to verify the effectiveness of the algorithm, simulations are conducted in MATLAB on a PC with the following configurations: 32 b Intel Core I5 CPU with 2.5 GHz frequency.

The initial velocity of UAV is 50 m/s, i.e., $C = 0.05$ km/s. The iteration step Δt of path planning is 1 s. The iteration step Δx_g of trajectory propagation is 1 m. In order to take full

advantage of terrain and make the path converge swiftly to the original streamline, sf = 1 in the following simulation. The ranges of repulsive and tangential parameter are $0.01 \leqslant \rho_0 \leqslant 30$ and $0.01 \leqslant \sigma_0 \leqslant 30$.

The aerodynamic data of selected UAV are listed in Table 1, where l is the wingspan of UAV and b_A the mean aerodynamic chord.

6.1. Comparison between the proposed method and IFDS method

Suppose the start point is $(0, 0, 0.5)$ km and the destination $(40, 40, 0.5)$ km. Six convex obstacles named as Obstacle I–Obstacle VI are constructed randomly in the planning space and the information of them is listed in Table 2.

Two methods are adopted here: one is the IFDS method[23] reckoning without tangential velocity; the other is the proposed method where attractive, repulsive and tangential velocity are all taken into account. When IFDS method is utilized, $\rho_0 = 1.0$ for each obstacle; when the proposed method is employed, $\rho_0 = 1.0$ and $\sigma_0 = 2.0$ for each obstacle.

Fig. 12 displays the path I and path II, which are correspondingly generated by the IFDS method and the proposed method. It is obvious that both paths can avoid obstacles smoothly and reach the destination eventually, but there are more vertical components of path I than path II. The error of dynamic pressure of two paths by trajectory propagation

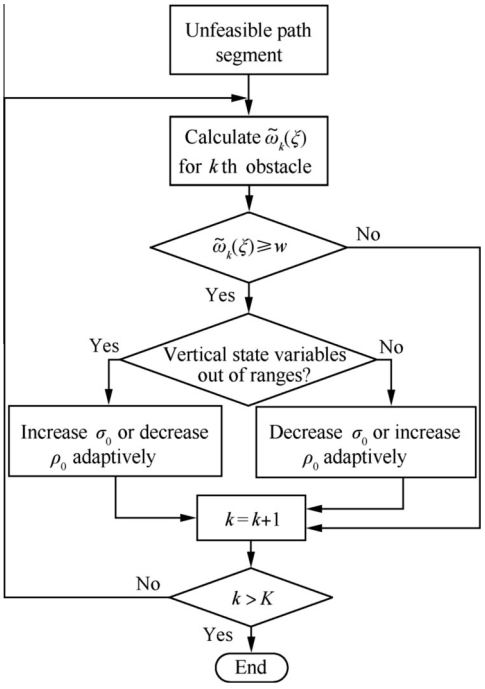

Fig. 11 Procedure of adjusting repulsive and tangential parameters.

Table 1 Aerodynamic data of selected UAV.

Parameter	Value
m (kg)	5000
S_w (m^2)	55.2
l (m)	30.0
b_A (m)	1.1
h (km)	[0.2, 4]
α (°)	[−3, 10]
γ (°)	[−30, 30]
μ (°)	[−10, 10]
ε (Pa)	0.001
ε' (Pa)	2

Table 2 Information of obstacles.

Obstacle	Information			
	Shape	Center	a, b, c	d, e, f
I	Sphere	(10, 10, 0)	4.5, 4.5, 4.5	1, 1, 1
II	Sphere	(10, 15, 0)	4.5, 4.5, 4.5	1, 1, 1
III	Cone	(18, 25, 0)	4.0, 4.0, 6.0	1, 1, 0.3
IV	Sphere	(20, 18, 0)	4.5, 4.5, 4.5	1, 1, 1
V	Cylinder	(30, 23, 0)	5.3, 5.3, 2.8	1, 1, 10
VI	Cone	(30, 35, 0)	3.5, 3.5, 6.5	1, 1, 0.4

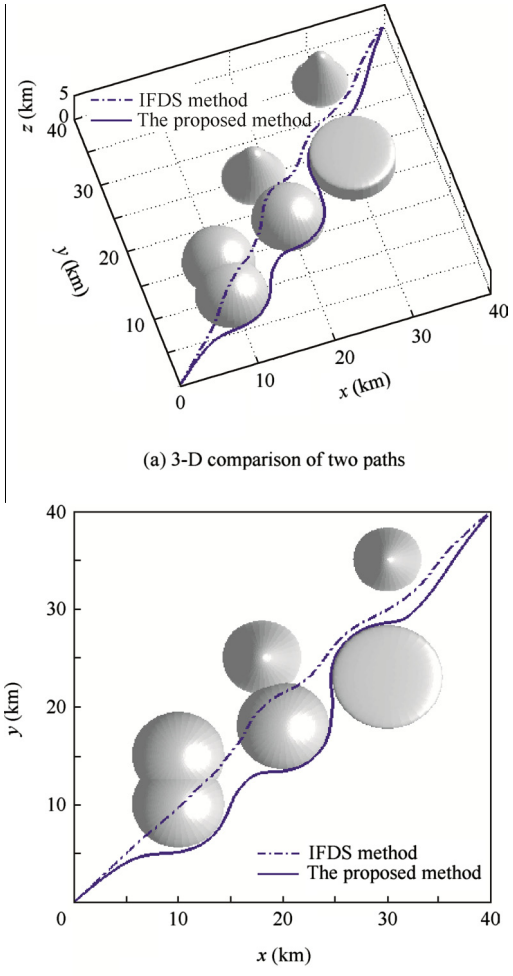

(a) 3-D comparison of two paths

(b) 2-D comparison in the x-y plane

Fig. 12 Planned paths of IFDS method and the proposed method.

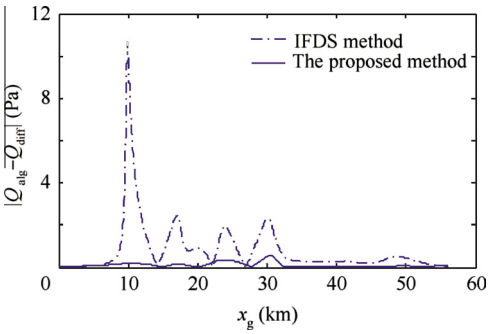

Fig. 13 Errors of dynamic pressure of two paths.

is shown in Fig. 13. $|Q_{alg} - Q_{diff}|$ of path I is out of range when 10 km $\leqslant x_g \leqslant$ 12 km, so path I is unfeasible; while $|Q_{alg} - Q_{diff}|$ of path II is within the range, so path II is flyable. The resolved state variables of the two paths are illustrated in Fig. 14, which can also explain the feasibility of two paths. Path I cannot satisfy the dynamic constraints of UAV as the flight-path angle μ is too big. For path II, the introduction of tangential velocity makes μ much smaller. Even though the heading angle φ and the bank angle γ are bigger than those of path I, they are still within the ranges.

The distribution of paths by IFDS method is limited. It is verified that even if we adjust ρ_0, the planned path in this environment is still unfeasible. For the proposed method, the

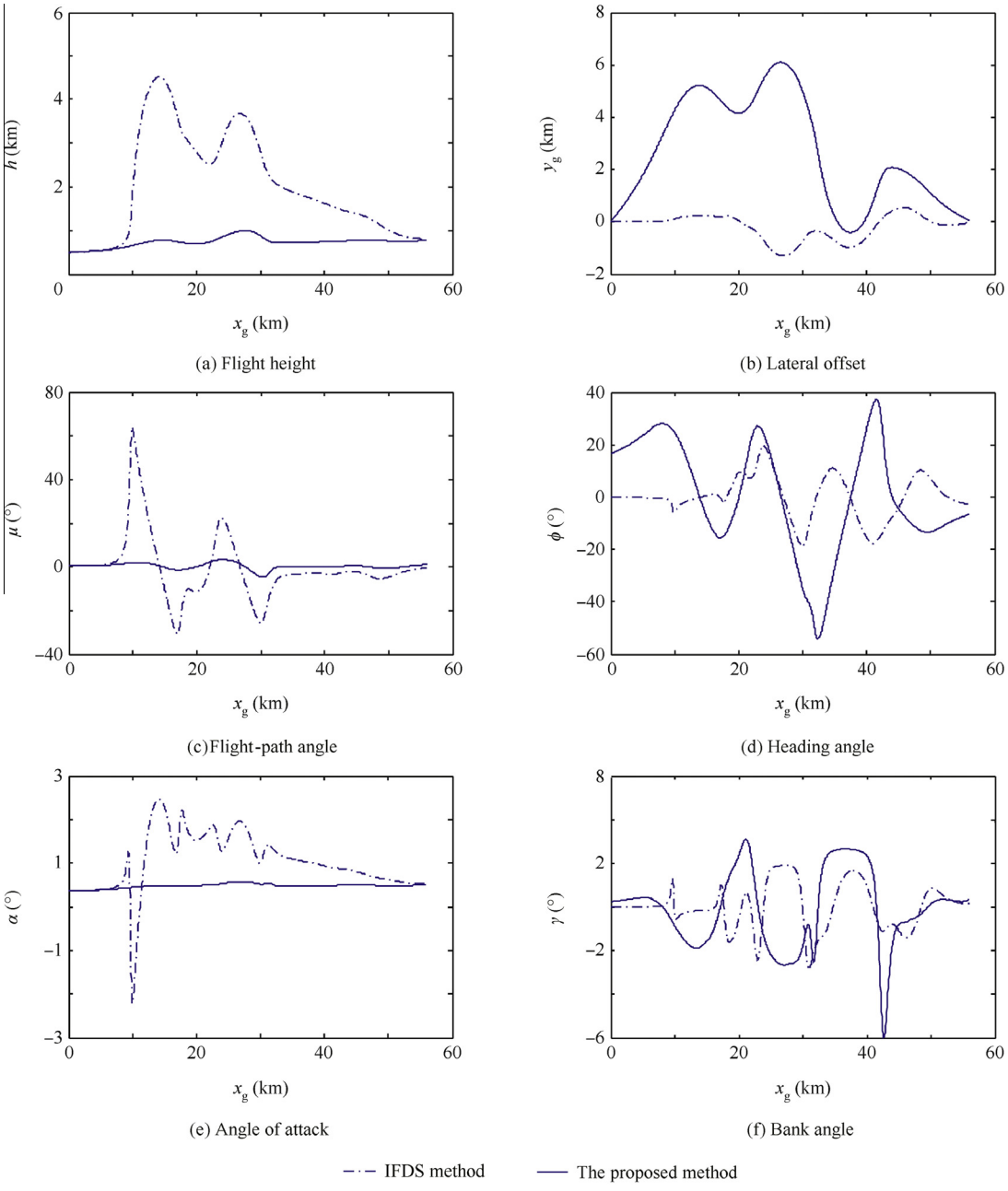

Fig. 14 Resolved state variables of two paths.

introduction of tangential velocity makes the streamlines fill in the whole planning space. By the adaption to repulsive and tangential parameter, it is much easier to obtain a feasible path.

6.2. Comparison between different parameters

Suppose there is one sphere, one cone and one cylinder in the environment. The start point is $(0, 0, 1.5)$ km and the target point is $(40, 0, 0.8)$ km. Assume that each obstacle has the same repulsive or tangential parameter, i.e., $\rho_{0,k} = \rho_0$ and $\sigma_{0,k} = \sigma_0$ $(k = 1, 2, \ldots, K)$. Define some evaluation indexes: L_{whole} is the whole length of path; $\min\{\text{dis}(O_1)\}$, $\min\{\text{dis}(O_2)\}$ and $\min\{\text{dis}(O_3)\}$ are the minimum distances between UAV and the surface of sphere, cone and cylinder obstacle respectively, and they represent the flight safety; $S_{\text{whole}} = \frac{1}{N-1}\sum_{n=2}^{N}|\langle V_n, V_{n-1}\rangle|$ denotes the global smoothness of path, where $\langle V_n, V_{n-1}\rangle$ means the angle between two path segments.

A group of repulsive and tangential parameters are chosen here. The corresponding paths are then planned, and the state variables and evaluation indexes of each path are listed in Table 3. By increasing ρ_0 or σ_0, the repulsive or tangential velocity increases, hence the path deflects earlier to avoid obstacles with a higher magnitude, as is shown in Fig. 15. Consequently UAV is safer but the cost of path length increases. When any parameter is too big, e.g., $\rho_0 = 1$, $\sigma_0 = 50$, $\rho_0 = 100$, $\sigma_0 = 1$ or $\rho_0 = 10$, $\sigma_0 = 1$, these paths with large L_{whole} are too conservative, seen from Table 3. When parameters are too small, e.g., $\rho_0 = 1$, $\sigma_0 = 0.1$, $\rho_0 = 0.01$, $\sigma_0 = 1$, the planned path is too close to the surface of obstacle. Considering the accuracy of obstacle information and the restriction of UAV maneuvering, UAV would be at the risk of crashing. Through the analysis, $\rho_0 = 1$, $\sigma_0 = 1$ is appropriate, as UAV is safe enough and the whole length of path is short. Meanwhile, the dynamic pressure error and the state variables are within their ranges. Although the global smoothness is worse than that of other groups, it is still acceptable.

Based on the above results, the repulsive and tangential parameters dominate the path quality. They can be selected ;appropriately depending on the specific flight mission.

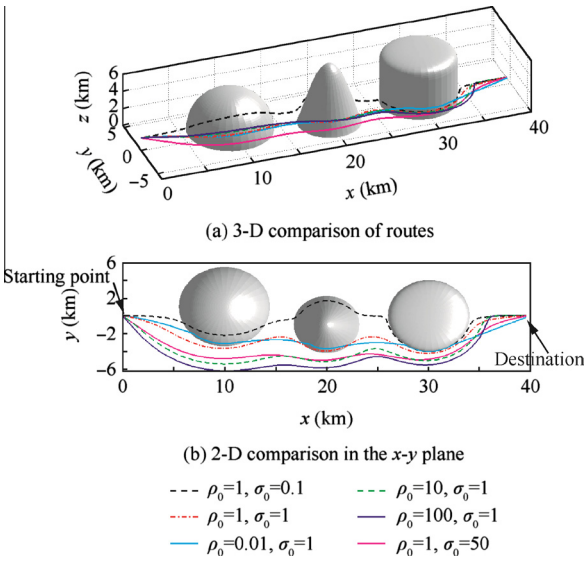

Fig. 15 Planned paths with different parameters.

6.3. Strategy of avoiding trap area

In order to verify the effectiveness of the strategy of avoiding trap area, two scenarios with trap area are constructed here.

In scenario 1, the start and target points are $(10, 10, 0.5)$ km and $(60, 60, 0.5)$ km. Four overlapping spheres produce the trap area, which UAV falls into eventually, as shown in Fig. 16(a). The planned path using the virtual target strategy is illustrated in Fig. 16(b). When UAV arrives at position $(29.52, 29.52, 0.50)$ km, the trap area is detected and a portion of sphere with radius 14 km is established, then the optimal virtual target is chosen as $(39.24, 39.24, 3.12)$ km, shown as an asterisk on the sphere. When UAV arrives at the virtual target, the target is reset to $(60, 60, 0.5)$ km.

In scenario 2, the start and target points of UAV are $(5, 5, 1.5)$ km and $(40, 40, 0.8)$ km. Three cone hills form the trap area in complex environment. In Fig. 17(a), UAV falls into the trap area. In Fig. 17(b), a portion of sphere with radius 11 km is established when UAV arrives at the position

Table 3 Information of planned paths.

Information	$\rho_0 = 100$	$\rho_0 = 10$	$\rho_0 = 1$	$\rho_0 = 0.01$	$\rho_0 = 1$	$\rho_0 = 1$
	$\sigma_0 = 1$	$\sigma_0 = 1$	$\sigma_0 = 1$	$\sigma_0 = 1$	$\sigma_0 = 50$	$\sigma_0 = 0.1$
h (km)	[0.79, 4.11]	[0.79, 3.56]	[0.80, 2.16]	[0.82, 1.71]	[0.81, 1.73]	[0.80, 3.42]
y_g (km)	[0, 6.19]	[0, 5.45]	[0, 3.56]	[0, 4.00]	[0, 5.04]	[0, 4.03]
μ (°)	[−11.45, 18.46]	[−11.37, 14.28]	[−8.76, 5.83]	[−3.49, 8.45]	[−3.42, 1.84]	[−26.11, 23.99]
φ (°)	[−69.20, 52.32]	[−64.97, 43.86]	[−52.35, 33.03]	[−27.29, 41.82]	[−43.51, 40.19]	[−64.79, 71.67]
α (°)	[0.45, 2.49]	[0.51, 2.09]	[0.52, 1.19]	[0.52, 6.02]	[0.52, 1.41]	[0.41, 1.85]
γ (°)	[−2.46, 23.12]	[−2.67, 16.04]	[−4.01, 6.28]	[−14.47, 25.03]	[−8.27, 22.95]	[−13.16, 33.66]
$\lvert Q_{\text{alg}} - Q_{\text{diff}}\rvert$ (Pa)	[0, 2.78]	[0, 2.25]	[0, 1.25]	[0, 1.03]	[0, 1.32]	[0, 2.06]
L_{whole} (km)	45.30	44.80	43.20	41.35	44.85	45.80
$\min\{\text{dis}(O_1)\}$ (km)	3.78	2.86	0.66	0.0001	1.60	0.17
$\min\{\text{dis}(O_2)\}$ (km)	2.42	1.66	0.39	0.0010	1.17	0.08
$\min\{\text{dis}(O_3)\}$ (km)	1.51	1.04	0.33	0.0014	0.79	0.03
S_{whole} (°)	0.3511	0.3865	0.4198	0.3679	0.2517	0.6638

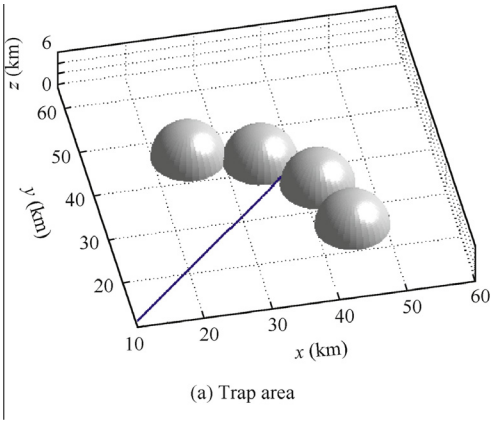

(a) Trap area

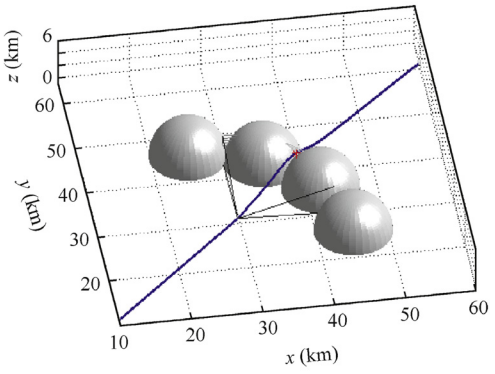

(b) Avoiding trap area with virtual target

Fig. 16 Avoiding trap area in scenario 1.

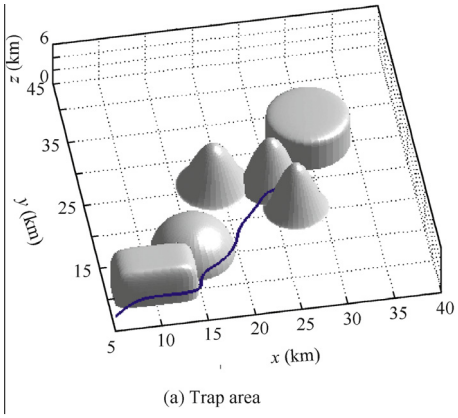

(a) Trap area

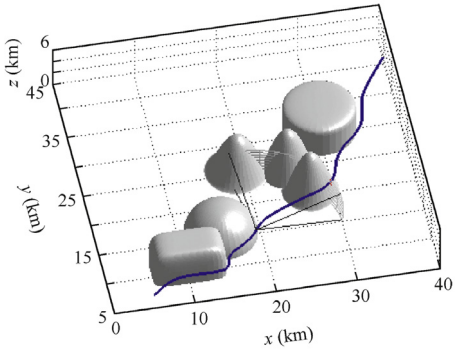

(b) Avoiding trap area with virtual target

Fig. 17 Avoiding trap area in scenario 2.

(19.05, 13.18, 1.71) km. The virtual target is determined as (28.96, 17.80, 2.98) km. And UAV can arrive at the destination eventually.

6.4. Strategy of avoiding obstacles with sharp edges

A scenario with some cuboids is assumed to simulate city environment here. As is known, the path by the proposed method is well shape-following. Fig. 18 illustrates the paths by IFDS and the proposed method in x–y plane. If we do not deal with the obstacles, the path is not feasible as it has some sharp turns, which is shown as path I . By smoothing the surface of obstacle, the planned path, i.e., path II is feasible and smooth. As UAV mainly flies on the horizontal plane in this scenario, the bank angle γ is the main criterion to judge whether the path is flyable. Fig. 19 shows the bank angles of the above paths resolved by trajectory propagation. The bank angle of path II is within the range $(-30°, 30°)$, while that of path I is out of range.

Compared with the strategy of smoothing the planned path,[20] the way of smoothing the obstacle can guarantee the impenetrability of the path. Besides, it is much easier and quicker to implement.

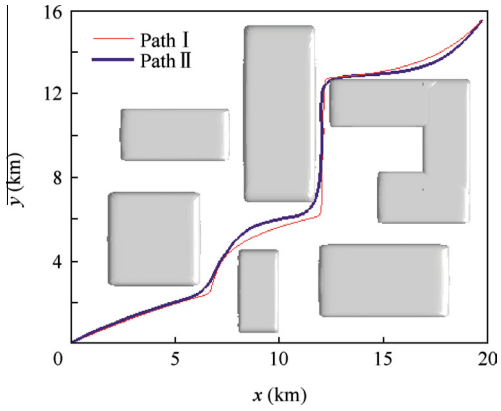

Fig. 18 Comparison of paths in x–y plane with IFDS method and the proposed method.

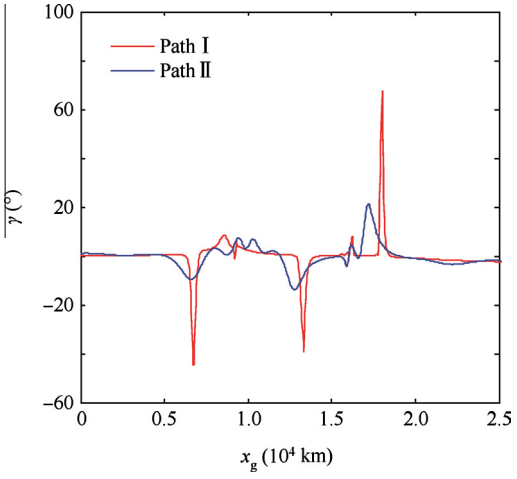

Fig. 19 Resolved bank angles of two paths.

6.5. Comparison between the proposed method and an improved APF method

In order to verify the effectiveness of the proposed method, it is compared with an improved APF method.[6] To ensure the uniformity, the distance between UAV and obstacle by APF method is replaced by $F(\xi)$. The step length of the APF method is also set to 0.05 km. For APF method, the scaling factor ζ of attractive potential and the scaling factor η of repulsive potential are eventually set to 0.2 and 0.1 respectively, by the contrast of simulations with different parameters. For the proposed method, the parameters of each obstacle are assumed to be $\rho_0 = 1.0,\ \sigma_0 = 3.0$ initially.

Assume the start point and the target point are $(10, 10, 1)$ km and $(42, 42, 1)$ km. Fig. 20 illustrates the paths by the two methods. The corresponding performance indicators are shown in Table 4. The state variables of two methods by trajectory propagation are shown in Table 5. Both paths can arrive at the target point eventually and avoid obstacles safely. However, there are severe deflections of the path by APF method when it gets close to the obstacles, which are marked by A, B, C, D and E respectively. By the proposed method, the quality of local paths near obstacles is significantly improved and the planned path is smoother and easier to track than the path generated by APF. Besides, the proposed method shows higher computational efficiency and has a smaller path cost.

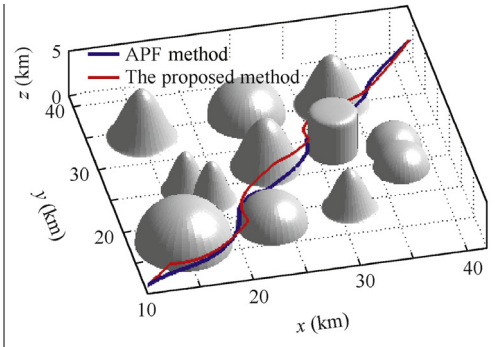

(a) 3-D comparison of two paths

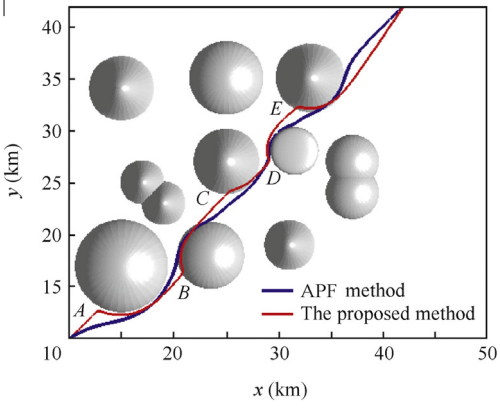

(b) 2-D comparison in the x-y plane

Fig. 20 Paths based on APF and the proposed method.

Table 4 Performance indicators of APF and the proposed method.

Parameter	Method	
	APF	The proposed method
Calculation time (s)	91.2	48.9
Waypoints	990	949
L_{whole} (km)	49.50	47.45
S_{whole} (°)	0.9392	0.3979

Table 5 State variables of paths by trajectory propagation.

State variable	Method	
	APF	The proposed method
h (km)	$[1.00, 2.65]$	$[0.75, 1.72]$
y_g (km)	$[-0.39, 3.39]$	$[-0.01, 3.26]$
μ (°)	$[-8.73, 9.86]$	$[-9.82, 6.34]$
φ (°)	$[-63.48, 70.85]$	$[-37.84, 32.54]$
α (°)	$[-3.39, 0.65]$	$[0.51, 1.00]$
γ (°)	$[-48.62, 48.58]$	$[-6.96, 5.66]$
$\lvert Q_{\text{alg}} - Q_{\text{diff}} \rvert$ (Pa)	$[0, 2.92]$	$[0, 1.25]$

7. Conclusions

The static 3-D path planning algorithm based on interfered fluid and trajectory propagation is investigated here. A feasible path can be obtained eventually in the complex environment.

(1) This path planning method is inspired by the flow disturbance. Especially, the tangential matrix is first introduced into the perturbation matrix. Therefore, it is easy to get a feasible path by adapting the repulsive or tangential parameter.
(2) The feasibility of path is judged by trajectory propagation, which is utilized by the match of dynamic pressure. As the method considers UAV dynamics, the path determined to be feasible can be tracked by UAV control system.
(3) The perturbation matrix is expressed by a simple formula, each part of which has intuitive definition. Hence good repulsive and tangential parameters can be guessed. Besides, the state variables of UAV, which are quickly resolved by trajectory propagation, provide some references for adjusting repulsive or tangential parameters. In general, the calculation of this algorithm is less than most methods.

In this paper, obstacles are static and known. The future work will take into account the path planning problem in dynamic environment.

Acknowledgments

This study was supported by the National Natural Science Foundation of China (No. 61175084) and the Program for Changjiang Scholars and Innovative Research Team in University of Ministry of Education of China (No. IRT13004).

References

1. Chitsaz H, LaValle SM. Time-optimal paths for a Dubins airplane. *Proceedings of the 46th IEEE conference on decision and control*; 2007 Dec 12–14; New Orleans. Piscataway, NJ: IEEE Press; 2007. p. 2379–84.
2. Hrabar S. 3D path planning and stereo-based obstacle avoidance for rotorcraft UAVs. *Proceedings of 2008 IEEE/RSJ international conference on intelligent robots and systems*; 2008 Sept 22–26; Nice, France. Piscataway, NJ: IEEE Press; 2008. p. 22–6.
3. Zucker M, Kuffner J, Branicky M. Multipartite RRTs for rapid replanning in dynamic environments. *Proceedings of 2007 IEEE international conference on robotics and automation*; 2007 Apr 10–14; Roma, Italy. Piscataway, NJ: IEEE Press; 2007. p. 1603–9.
4. Khaitib O. Real-time obstacle avoidance for manipulators and mobile robots. *Internat J Rob Res* 1986;**5**(1):90–8.
5. Jaradat MAK, Garibeh MH, Feilat EA. Autonomous mobile robot dynamic motion planning using hybrid fuzzy potential field. *Soft Comput* 2011;**16**(1):153–64.
6. Saravanakumar S, Asokan T. Multiple potential field method for path planning of autonomous underwater vehicles in 3D space. *Intell Service Rob* 2013;**6**(4):211–24.
7. Agirrebeitia J, Aviles R, de Bustos IF, Ajuria G. A new APF strategy for path planning in environments with obstacles. *Mech Mach Theory* 2005;**40**(6):645–58.
8. Dong ZN, Zhang RL, Chen ZJ, Zhou R. Study on UAV path planning approach based on fuzzy virtual force. *Chin J Aeronaut* 2010;**23**(3):341–50.
9. Lam TM, Boschloo HW, Mulder M, van Paassen MM. Artificial force field for haptic feedback in UAV teleoperation. *IEEE Trans Syst Man Cybern Part A: Syst Humans* 2009;**39**(6):1316–30.
10. Fu YG, Ding MY, Zhou CP. Phase angle-encoded and quantum-behaved particle swarm optimization applied to three-dimensional route planning for UAV. *IEEE Trans Syst Man Cybern Part A: Syst Humans* 2013;**43**(6):1451–65.
11. Roberge V, Tarbouchi M, Labonte G. Comparison of parallel genetic algorithm and particle swarm optimization for real-time UAV path planning. *IEEE Trans Indust Inf* 2013;**9**(1):132–41.
12. Chen M, Wu QX, Jiang CS. A modified ant optimization algorithm for path planning of UCAV. *Appl Soft Comput* 2008;**8**(4):1712–8.
13. Zhang XY, Duan HB. An improved constrained differential evolution algorithm for unmanned aerial vehicle global route planning. *Appl Soft Comput* 2015;**26**(1):270–84.
14. Tong H, Chao WW, Qiang HC, Bo XY. Path planning of UAV based on Voronoi diagram and DPSO. *Proc Eng* 2012;**29**(1):4198–203.
15. Ozalp N, Sahingoz OK. Optimal UAV path planning in a 3D threat environment by using parallel evolutionary algorithms. *Proceedings of 2013 international conference on unmanned aircraft systems (ICUAS)*; 2013 May 28–31; Atlanta, USA. Piscataway, NJ: IEEE Press; 2013. p. 308–17.
16. Pehlivanoglu YV. A new vibrational genetic algorithm enhanced with a Voronoi diagram for path planning of autonomous UAV. *Aerosp Sci Technol* 2012;**16**(1):47–55.
17. Khansari-Zadeh SM, Billard A. A dynamical system approach to realtime obstacle avoidance. *Auton Rob* 2012;**32**(1):433–54.
18. Karimi J, Pourtakdoust SH. Optimal maneuver-based motion planning over terrain and threats using a dynamic hybrid PSO algorithm. *Aerosp Sci Technol* 2013;**26**(1):60–71.
19. Mattei M, Blasi L. Smooth flight trajectory planning in the presence of no-fly zones and obstacles. *J Guidance Control Dyn* 2010;**33**(2):454–62.
20. Liang X, Wang HL, Li DW, Lyu WT. Three-dimensional path planning for unmanned aerial vehicles based on principles of stream avoiding obstacles. *Acta Aeronaut Astronaut Sin* 2013;**4**(7):1670–81 [Chinese].
21. Liang X, Wang HL, Li DW, Liu C. Three-dimensional path planning for unmanned aerial vehicles based on fluid flow. *Proceedings of 2014 IEEE aerospace conference*; 2014 Mar 1–8; Montana, America. Piscataway, NJ: IEEE Press; 2014. p. 1–13.
22. Sullivan J, Waydo S, Campbell M. Using stream functions for complex behavior and path generation. *Proceedings of AIAA guidance, navigation and control conference*; 2003 Aug 11–14; Austin, Texas. Reston: AIAA; 2003. p. 1–9.
23. Ye GH, Wang HO. Managing group behaviors in swarm systems by associations. *Proceedings of the 2006 American control conference*; 2006 Jun 14–16; Minnesota, USA. Piscataway, NJ: IEEE Press; 2006. p. 3537–44.
24. Wang HL, Lyu WT, Yao P, Liang X, Liu C. Three-dimensional path planning for unmanned aerial vehicle based on interfered fluid dynamical system. *Chin J Aeronaut* 2015;**28**(1):229–39.
25. Yao P, Wang HL, Liu C. 3-D dynamic path planning for UAV based on interfered fluid flow. *Proceedings of 2014 IEEE Chinese guidance, navigation and control conference*; 2014 Aug 12–14; Yantai, China. Piscataway, NJ: IEEE Press; 2014. p. 997–1002.
26. Gregg HB, Steven GT. Automatic trajectory design for the X-34. 1999. Report No.: AIAA-1999-4161.
27. Wang HL, Su ZK, Pei YF. Design of landing trajectory and safe interface area for RLV with initial interface errors. *Acta Aeronaut Astronaut Sin* 2014;**35**(11):3092–105 [Chinese].
28. Zhang Y, Chen J, Shen LC. Real-time trajectory planning for UCAV air-to-surface attack using inverse dynamics optimization method and receding horizon control. *Chin J Aeronaut* 2013;**26**(4):1038–56.
29. Liang Y, Qi JT, Xiao JZ. A literature review of UAV 3D path planning. *Proceedings of 2014 11th world congress on intelligent control and automation*; 2014 Jun 20–Jul 4; Shenyang, China. Piscataway NJ: IEEE Press; 2014. p. 2376–81.
30. Benallegue M, Escande A, Miossec S, Kheddar A. Fast C^1 proximity queries using support mapping of sphere-torus-patches bounding volumes. *Proceedings of 2009 IEEE international conference on robotics and automation*; 2009 May 12–17; Kobe, Japan. Piscataway, NJ: IEEE Press; 2009. p. 483–8.
31. Zhang CG, Xi YG. Mobile robot path planning based on rolling windows. *Syst Eng Electron* 2002;**24**(6):63–9 [Chinese].

Yao Peng is currently a Ph.D. candidate in Navigation, Guidance and Control, School of Automation Science and Electrical Engineering, Beihang University. His research interests include theory and method of path planning in complex environments for unmanned aerial vehicle (UAV) and autonomous flight control for UAV.

Wang Honglun received the B.S., M.S., and Ph.D. degrees in Fire Control from Northwestern Polytechnical University, China, in 1992, 1995 and 1998. From 1998 to 2000, he did his postdoctoral research at Nanjing University of Aeronautics and Astronautics, China. In 2000, he joined the Unmanned Aerial Vehicle Research Institute, Beihang University, as a professor affiliated with Navigation, Guidance and Control. He was chosen by the New Century Excellent Researcher Award Program from Ministry of Education of China in 2009. His research interests include autonomous flight control for unmanned aerial vehicles (UAV), perception and obstacle-avoidance technology for UAVs, as well as theory and method of path planning in complex environments for UAVs.

Su Zikang is currently a Ph.D. candidate in Navigation, Guidance and Control, School of Automation Science and Electrical Engineering, Beihang University. His research interests include intelligent control of nonlinear systems and its application of advanced control and optimization techniques to aerospace.